Summer 2024

Sub-Critical Crack Growth and Fatigue Behaviour of Alkali Silicate Glass

Noah Weyrauch
Missouri University of Science and Technology

Department:

SUB-CRITICAL CRACK GROWTH AND FATIGUE BEHAVIOUR OF ALKALI SILICATE GLASS

by

NOAH MICHAEL WEYRAUCH

A THESIS

Presented to the Graduate Faculty of the

MISSOURI UNIVERSITY OF SCIENCE AND TECHNOLOGY

In Partial Fulfillment of the Requirements for the Degree

MASTER OF SCIENCE IN MATERIAL SCIENCE AND ENGINEERING

2023

Approved by:

Richard K. Brow, Advisor
F. Scott Miller
Jeremy L. Watts
Kevin T. Strong Jr.

ABSTRACT

Delayed failure in silicate glasses can be linked to subcritical crack growth (SCCG) where surface defects grow over time until catastrophic failure. This phenomenon originates from stress-enhanced chemical interactions between the environment (e.g. water) and the strained silicate bonds at the crack tip. SCCG must be accounted for to predict the long-term survivability of silicate-glass components. This study compares two methods to measure SCCG parameters for a commercial alkali silicate sealing glass and for a series of binary xNa_2O-$(1-x)SiO_2$ glasses, where $0.15 \leq x \leq 0.35$. A constant moment double cantilever beam (DCB) technique was used to directly measure the three regions of crack velocity (v) as a function of stress intensity (K_I) to describe the conditions of SCCG up to catastrophic failure. The two-point bend (TPB) method was used to determine failure strains as functions of relative humidity for fibers drawn from melts of the same glasses. The fatigue parameters calculated from the dependence of failure strain on the TPB faceplate velocity were then compared with those obtained from the direct velocity measurements by using a power-law model to calculate the Region I crack velocity.

ACKNOWLEDGMENTS

I would like to extend my deepest gratitude to my research advisor, Dr. Richard K. Brow. Dr. Brow's leadership, guidance and dedication propelled this project from start to finish. Dr. Brow possesses an uncanny enthusiasm for experimentation which inspired me to continue to challenge myself throughout the project. Dr. Brow's eagerness, knowledge, and character are important traits of an excellent advisor, and I am eternally thankful to have had him as mine.

Next, I would like to thank Taylor Murphy, my undergraduate research assistant, for collecting many of the two-point bend data sets and for having a positive attitude towards the project. I also wish to thank my lab peers in Dr. Brow's group for their collaborations over the past two years. Finally, I am grateful for Fred Eickelmann and the other MRC staff members for their technical support.

I would be remiss without thanking Dr. Kevin T. Strong Jr. and the rest of the LDRD team at Sandia National Laboratories/Albuquerque, for their in-depth partnership, advice, and financial support. I am also grateful to Thomas Diebold and Jonah Carmichael for all the technical support and direction they offered while I was conducting experiments both at Missouri S&T and at SNL.

Finally, I must express my very profound gratitude to my parents and siblings for providing me with unfailing support and continuous encouragement throughout my years of study and through the process of researching and writing this thesis. To my friends, this would have been a far more difficult feat without you and thanks for all the fun and support along the way.

TABLE OF CONTENTS

Page

LIST OF ILLUSTRATIONS

Page

LIST OF TABLES

Page

NOMENCLATURE

Symbol	Description
E	Young's modulus
c	Size of flaw
γ	Surface energy
σ	Strength
K_I	Stress intensity
K_{IC}	Fracture toughness
ν	Crack velocity
G	Strain energy release rate
M	Bending moment
I	Moment of inertia
t	Groove thickness (DCB)
b	Sample thickness (DCB)
h	Half width (DCB)
a	Groove depth (DCB)
w	Half of groove width (DCB)
d	Fiber diameter
v_{fp}	Faceplate velocity
D	Distance at failure (TPB analysis)
ε_f	Failure strain
n	Fatigue parameter

n_{TP}	Dynamic fatigue parameter from TPB
T_{melt}	Melting temperature
t_{melt}	Melting time
T_{anneal}	Annealing temperature
t_{anneal}	Annealing time
P	Probability of failure
m	Weibull modulus
T_g	Glass transition temperature
n_{DCB}	Dynamic fatigue parameter from DCB
A	Subcritical crack growth parameter
A^*	Slow crack growth parameter
σ_i	Inert strength
α	Slope of the log(flexure strength) vs. log(stress rate)
β	Y-intercept of the log(flexure strength) vs. log(stress rate)
Y	Geometry factor related to flaw shape
B	Material/environmental parameter
r	Radius of fiber

1. INTRODUCTION

1.1. OVERVIEW OF GLASS STRENGTH

For many applications of silicate glasses, such as windows, displays for electronic devices, and pharmaceutical containers, fracture strength limits performance and functionality. The practical strength of glass depends on the interaction of water with glass structure which controls the conditions for subcritical crack growth (SCCG). Although commercial glass compositions are often more complicated, binary sodium silicate glasses can serve as representative models for these multicomponent silicate glasses and information on these simpler glasses can be used as a foundation for a range of experimental and computational studies.[1]

By treating glass as a flawless brittle solid, its theoretical strength can be predicted from the amount of work done to pull bonds apart to create two new surfaces, and that theoretical strength has been predicted to be in the range of E/10 to E/π, where E is Young's modulus.[2] Fused silica has an elastic modulus of 70 GPa, leading to predictions of theoretical strength of 13 to 30 GPa,[3] and studies of pristine silica fibers have reported tensile strengths in the range of 9-14 GPa.[4] However, practical glass surfaces are not flaw-free. For real world applications of glass, the theoretical strength is greatly reduced by strength-limiting flaws that form from processing, machining, and handling.[5] In addition, environmental interactions with the glass also degrade the strength of glass, as will be discussed in more depth later.

1.2. EFFECT OF FLAWS

Fracture strength is a function of a number of parameters including elastic modulus (E, GPa), flaw size (c, m), and fracture surface energy (γ, J/m^2). Griffith used an energy-balance analysis that related the loss in strain energy at fracture to the gain in surface energy.[5] He modeled elliptical flaws in an infinite plate that concentrated strain energy at the flaw tip to predict fracture strength (σ, GPa) for brittle materials, according:

$$\sigma = \sqrt{2E\gamma/\pi c} \quad [1]$$

Since flaw size can vary widely, the strength of glass is considered an extrinsic property that depends on how the material is processed and handled. Table 1.1 shows representative strengths based on handling conditions.[6]

Table 1.1: Typical strength of glass samples based on experience.[6]

Sample Conditioning	Typical Strength
Freshly drawn, pristine fibers	~700-10,000 MPa
Handled fibers	~350-700 MPa
Freshly drawn rods	~70-140 MPa
Abraded rods	~14-35 MPa
Used glass products	~14-70 MPa

There are three types of modes of loading that will produce cracks in a material, distinguished by the direction the load is being applied (Figure 1.1). Mode I is an opening (tensile) mode, mode II is an in-plane crack shearing mode, and mode III describes an anti-plane shearing or tearing crack.[7]

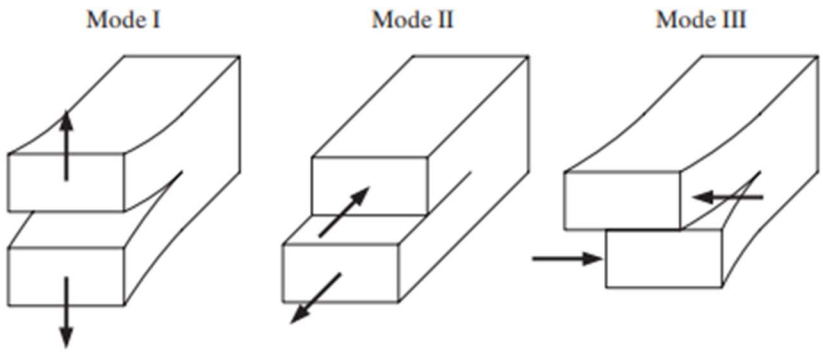

Figure 1.1: Mode I, II, and III fracture geometries, adapted from Wachtman et al.[7]

Mode I is the most common loading mode and corresponds to the stress intensity factor K_I (MPa•m$^{1/2}$). Stress intensity factors are used to predict the stress state at or near the crack tip caused by residual stress or an applied load (σ, Pa):

$$K_I = \sigma\sqrt{\pi c} \quad [2]$$

where c is the half size of the crack (m). When the stress state becomes critical (K_{IC}), the crack will grow at critical speeds until failure. Fracture toughness, K_{IC}, is a mechanical property that describes the ability of a material to resist fracture. For loads less than K_{IC}, crack propagation occurs but at slower velocities, as discussed below.

1.3. DOUBLE CANTILEVER BEAM STUDY

A test often used to analyze crack propagation is the double cantilever and double torsion test.[8-12] The configuration of the applied moment double cantilever beam (DCB) specimen is shown in Figure 1.2. The central groove machined down the entirety of the specimen guides the crack, keeping it centered as it travels down the sample.[13] The dimensions of the samples are designed to prevent the fracture stress applied by the

specimen arms from becoming critical. When the cantilever beam is subjected to the applied bending moment, deformation occurs in the form of a crack at the central notch.[5]

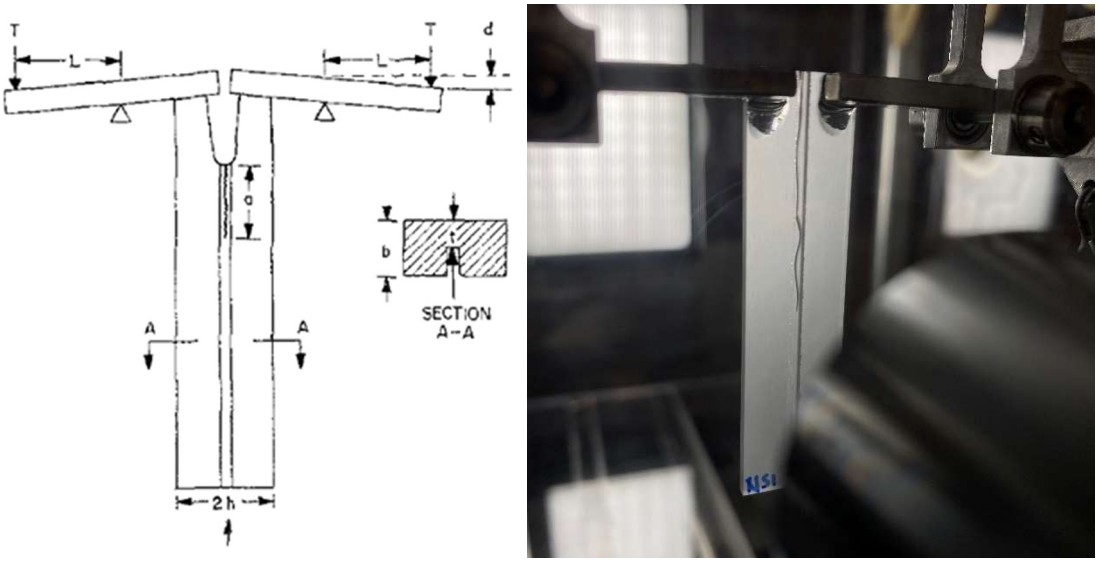

Figure 1.2: (left) Schematic drawing of the constant double cantilever beam test, adapted from Freiman et al.[5] and (right) a photograph of a DCB sample from the present study.

The constant moment DCB technique can be used to directly measure crack velocity (ν) as a function of stress intensity. The strain energy release rate, $\mathcal{G}$, is independent of crack length and can be used to calculate K_I in relation to the changes of crack velocity:

$$\mathcal{G} = \frac{M^2}{EIt} \quad [3]$$

$$K_I = \sqrt{\mathcal{G}E} \quad [4]$$

Here, M is the bending moment, E is the elastic modulus of the glass, I is the moment of inertia, and t is the groove thickness. The moment of inertia was calculated using Equation 5, which accounts for the central groove.[13]

$$I = \frac{bh^3 - aw^3}{3} - \frac{\left(bh^2 - aw^2\right)^2}{4(bh - a\ )} \quad [5]$$

Here, b is the sample thickness, h is one-half of the sample width, a is the depth of groove, and w is one-half of the groove width.

1.4. SUBCRITICAL CRACK GROWTH

Subcritical crack growth often precedes fracture in a glass or ceramic material, where crack extension originates and propagates from micro-flaws within the material or on the sample surface. Subcritical crack growth is a result of a stress-enhanced chemical reaction between the material and moisture in the surrounding environment. This has been observed in glasses, traditional ceramics such as porcelains, oxides, and silicate minerals.[14] Much of the available crack propagation data has been collected on glasses because their transparent nature makes optical monitoring of the crack tip easier than what it would be for most opaque ceramic materials.

Subcritical crack growth can be divided into four major regions (Figure 1.3). Region 0 occurs below the stress intensity threshold, the load below which no crack propagation occurs.[15] Region I shows a consistent increase in crack velocity with increasing applied load and is controlled by a stress-enhanced chemical reaction between water and the glass.[16,17] Region II is a plateau in the dependence of crack velocity on the applied load, where the growth rate is now determined by the rate at which water can be transported to the crack tip.[18] In Region III, crack velocity increases significantly, progressing at rates that no longer depend on the presence of water, as shown by comparisons of crack velocities measured in vacuum and in water.[19, 20]

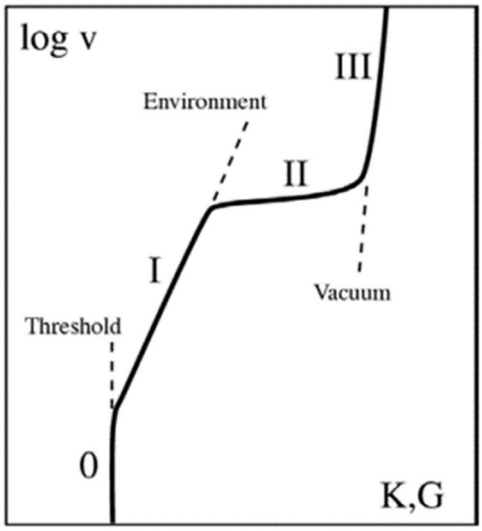

Figure 1.3: Four regions of subcritical crack growth adapted from Ciccotti.[21]

Region I is the stress-corrosion regime and SCCG here is attributed to the stress-enhanced chemical reaction between water and the glass,[16,17] where water and glass composition (Figure 1.4) affect the dependence of crack velocity on the applied load.

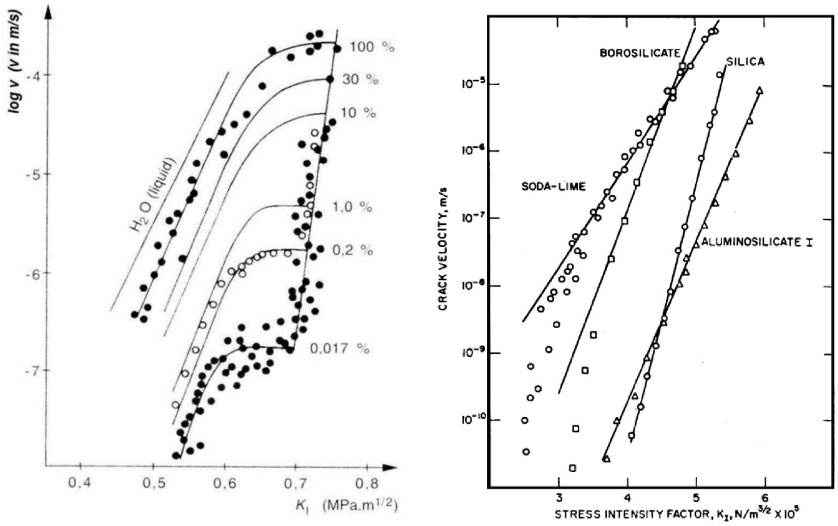

Figure 1.4: (left) Effect of humidity on crack propagation in soda-lime glass, and (right) Region I crack propagation in commercial glasses; adapted from Wiederhorn.[22, 23]

Stress corrosion cracking is one of the most important causes of failure of brittle materials. The strength of glass is reduced not only by the presence of flaws but also by environmental fatigue, the stress-enhanced chemical reactions that occur at a flaw tip. Water in the environment, even in small quantities, reduces the strength of the glass under load over time, a process called static fatigue. Wiederhorn showed that static fatigue only occurred in the presence of water and that the water vapor produced a corrosive attack on the glass at the crack tip in Region I and II. Wiederhorn also found that samples tested in vacuum or in dry nitrogen had strengths that were independent of water vapor, similar to what was observed in Region III.[24]

The phenomenon of delayed failure of brittle materials was first described as static fatigue by Baker and Preston in 1946, who emphasized the influence of humidity on failure characteristics.[25-27] Since static fatigue is due to crack growth, the environment at the crack tip and the reactions that occur there play a larger role in determining the strength of the glass. For this reason, fatigue should be considered for any application of glass, in air or in aqueous environments, when load is being applied.

Stress-corrosion is thought to be the main mechanism for failure of glasses due to the chemical reaction between the water and the strained bonds at the crack tip.[22] Silica is considered to be inert in water when under no strain, but when the Si-O-Si bond is strained, it reacts with the water and hydrolyzes:[28-29]

$$\begin{matrix} | & | \\ -Si-O-Si- \\ | & | \end{matrix} + H_2O \rightarrow \begin{matrix} | \\ -O-Si-OH \\ | \end{matrix} \quad \begin{matrix} | \\ HO-Si-O- \\ | \end{matrix} \qquad [6]$$

In more basic solutions, silica is more susceptible to fatigue because hydroxyl ions can further attack the siloxane bonds that constitute the glass network,[30] to further propagate crack growth and sharpen the crack tip.[21]

$$-\overset{|}{\underset{|}{Si}}-O-\overset{|}{\underset{|}{Si}}-+OH^- \rightarrow -\overset{|}{\underset{|}{Si}}-O^- + -\overset{|}{\underset{|}{Si}}-OH \qquad [7]$$

The development of silanol bonds on the crack surfaces (e.g., reactions 6 and 7) can also affect the chemistry of the solution at a crack tip which in turn affects crack growth[31].

For alkali-containing glasses, the solution at the crack tip is altered by an ion exchange reaction between the alkali ions and hydrogen ions in the solution, increasing pH at the crack tip which further etches the glass.[32]

$$-\overset{|}{\underset{|}{Si}}-O-Na^+ \;\; Na^+-O-\overset{|}{\underset{|}{Si}}- \rightarrow -\overset{|}{\underset{|}{Si}}-OH \; HO-\overset{|}{\underset{|}{Si}}-O \qquad [8]$$

Doremus suggested the possibility that hydronium (H_3O^+) ions are involved in the ion-exchange process as well.[33] Depth profile studies of hydrated soda-lime silicate glass found that three hydrogen atoms replaced each Na atom that had leached from the hydrated glass surface, consistent with a Na^+-H_3O^+ exchange mechanism:

$$-\overset{|}{\underset{|}{Si}}-O^-Na^+ + H_3O^+ \rightarrow -\overset{|}{\underset{|}{Si}}-OH + H_2O + Na^+ \qquad [9]$$

Charles credited the fatigue in sodium silicate glasses to the extension of surface flaws by the leaching of Na^+ ions from the glass at the crack tip.[34-36] France et al. studied the fatigue of silica and sodium borosilicate glasses in air and in water.[37] For samples tested in water, they found that glasses with low-soda contents were less susceptible to fatigue. Wiederhorn and Boltz studied stress corrosion for several different glass compositions and found that

silica glass had the greatest resistance to stress corrosion followed by other low-alkali containing glasses, as seen in Figure 1.4, right. Soda-lime silicate glass, on the other hand, was much more sensitive to stress corrosion effects, indicating that reactions like those shown in equations [8 and 9] contribute to fatigue.[31] From this Wiederhorn developed a model for the dependence of Region I crack velocity on humidity (Figure 1.4, left)[22] and this model is the basis of the analysis that will be used later in this document.

1.5. TWO-POINT BEND STUDY OF FATIGUE

A common method for testing mechanical properties of high strength fibers are loading in tension and in two-point bending (TPB).[38] Unlike the tensile test, the two-point bend method does not present significant gripping problems and so is relatively easy to do. However, TBP measures failure strain, not stress, and so without information about the strain-dependence of the elastic modulus, TBP data cannot be used to measure strength.[38]

In a TPB test (Figure 1.5), a section of glass fiber with diameter, d (μm), is bent into a U-shape between two parallel faceplates, one which is stationary and the other that travels at a programed faceplate velocity (v_{fp}), compressing the 'U' shaped fiber until failure. The assembly is halted by an acoustic sensor that picks up the sound of the fiber failing. The gap distance at failure (D, μm) is recorded, and the failure strain (ε_f) is calculated with the following equation: [39]

$$\varepsilon_f = \frac{1.198 \times d}{(D-d)} \qquad [10]$$

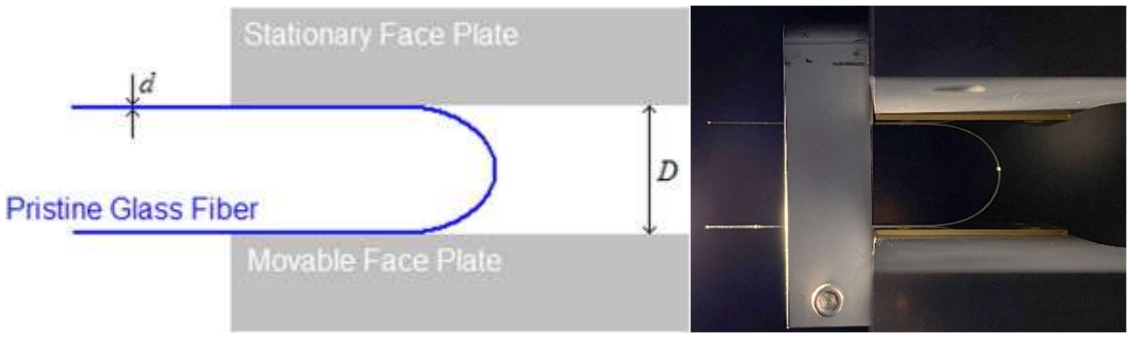

Figure 1.5: (left) Schematic diagram of the two-point bending test configuration, and (right) a photo of a fiber between the faceplate assembly used in the present study; adapted from Tang and Brow.[40]

Previous TPB studies have been done to characterize dependence of failure strain on humidity, an example of which is shown in Figure 1.6.[40] Water activity clearly has an effect on failure strain.

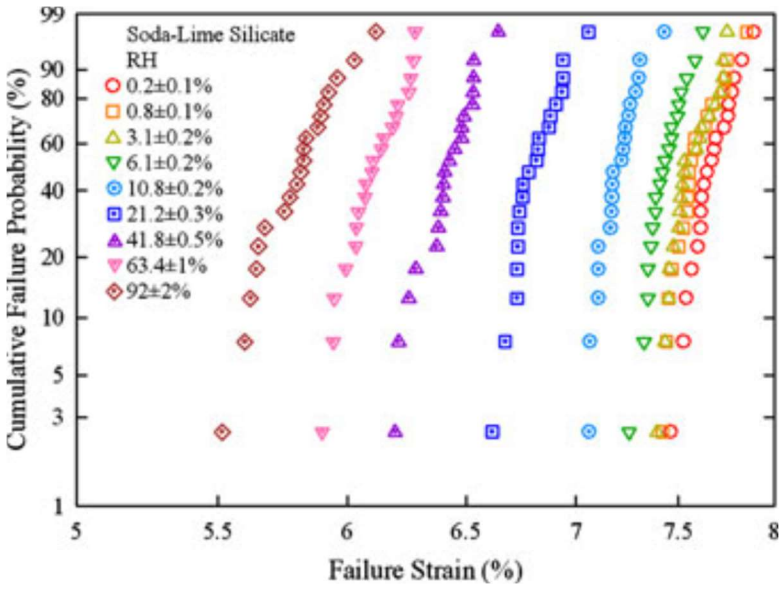

Figure 1.6: Two-point bend failure strains in air at different relative humidities for soda-lime silicate glass, from Tang et al.[40]

A dynamic fatigue parameter, n, is typically measured from failure stress or strain measurements at different loading rates.[41] Rondinella and Matthewson compared three different loading modes in a TPB experiment (constant faceplate velocity (v_{fp})), constant strain rate, and constant stress rate, and found similar dependences for failure strains.[42] From these studies, they derived the TPB dynamic fatigue parameter, n_{TPB}, as:

$$n_{TPB} = 1 + 1/\left(\frac{d\log(\varepsilon_f)}{d\log(v_{fp})}\right) \quad [11]$$

1.6. SUMMARY OF PROJECT

Brittle material failure can appear random and unpredictable when stresses are at a subcritical level, below fracture toughness. Gaps in our understanding of how structural flaws and environmental factors, particularly humidity, impact fracture propagation need to be better understood.

In the present study, fatigue-related information was obtained for a commercial silicate glass and a series of binary sodium silicate glasses. The DCB method was used to measure crack velocities in Regions I, II, and III, and the TPB method was used to measure the fatigue parameters in water and in air at different values of RH for the same glasses. The two sets of measurements were compared using a power law model.

2. METHODOLOGY

2.1. MATERIAL SELECTION

A series of sodium silicate glasses with the nominal molar composition $xNa_2O\cdot(100-x)SiO_2$, where x = 15, 20, 25, 30, and 35, were produced with Na_2CO_3 (Fisher Science, ≥99.5% purity) and SiO_2 (Alfa Aesar, 99.5% purity) as raw materials that were mixed and then melted in a platinum-rhodium crucible in air using the conditions summarized in Table 2.1. The melts were stirred with a platinum rod every hour for 3 hours, then left undisturbed for the final hour to allow any remaining bubbles to escape. Melts were poured into a 64x100 mm preheated (150°C) graphite mold and annealed at $T_{anneal,1}$ for two hours, cooled and held at $T_{anneal,2}$ for two more hours, then cooled to room temperature. Schott-8061 glass monoliths, received from the manufacturer, were remelted, cast and annealed using the conditions indicated in Table 2.1.

Table 2.1: Melting temperature (T_{melt}), melting time (t_{melt}), annealing temperature (T_{anneal}), and annealing time (t_{anneal}) for glasses prepared in the laboratory.

Glass Composition	T_{melt} (°C)	t_{melt} (hr)	$T_{anneal,1}$ (°C)	$t_{anneal,1}$ (hr)	$T_{anneal,2}$ (°C)	$t_{anneal,2}$ (hr)
$15Na_2O\cdot85SiO_2$	1650	4	485	2	435	2
$20Na_2O\cdot80SiO_2$	1500	4	480	2	430	2
$25Na_2O\cdot75SiO_2$	1500	4	470	2	420	2
$30Na_2O\cdot70SiO_2$	1300	4	460	2	410	2
$35Na_2O\cdot65SiO_2$	1250	4	450	2	400	2
Schott 8061	1500	4	460	2	410	2

Annealed glasses were machined (Bomas Machine Specialties, Inc., Woburn, MA) into one of five different types of samples for mechanical testing; sample dimensions are given in Table 2.2. The double-cantilever beam (DCB) samples were also machined with a 1.25 mm width central square groove down the length of each sample at a depth of 0.65 mm. Samples were machined in aqueous based cleaning fluid.

Table 2.2: Geometries of samples prepared for mechanical testing.

Sample	Dimensions
ASTM C1421 Bend Bars	3 mm x 4 mm x 50 mm
Constant Moment DCB	1.5 mm x 12.7 mm x 50.8 mm
DMA specimen	3 mm x 4 mm x 50 mm
Fibers	12.5 cm long, 100 mm diameter
TMA/RUS specimen	10 mm x 10 mm x 25 mm

Glass fibers were drawn from the surfaces of the Na-silicate and S-8061 glass melts using a process described elsewhere.[43] Briefly, bubble-free melts were heated in a platinum crucible to the fiber-pulling temperature (melt viscosity about 10^4 Pa-s, Table A.1), and a fiber was drawn from the melt surface and attached to a rotating cage positioned above the melt. The cage then pulled continuous fibers about 100 μm in diameter (Table 2.2). Because the cage rotated on a screw, the fibers were separated as they were drawn to produce pristine samples about 12.5 cm long when cut from the cage arms. These fibers were used in the two-point bending experiments described below.

2.2. SUBCRITICAL CRACK GROWTH

Subcritical crack growth velocities were measured using a constant moment double cantilever beam (DCB) setup, similar to that described by Freiman.[5] A two-part epoxy (Devcon) was used to attach the metal arms to the glass sample which was then notched using a 0.5 mm wide slow speed diamond saw to introduce an initial flaw for crack propagation. Notched samples were attached to the bending moment assembly inside a plexiglass environmental chamber. The initial DCB measurements on Schott-8061 samples were done in 20°C air with a relative humidity (RH) fixed at 75±5% RH using a saturated salt solution (36:100 NaCl:deionized water by mass) held in an open container in the chamber; the RH was monitored by a hygrometer (Electro Tech Systems Inc., Glendale, PA). The environmental chamber was subsequently equipped with two inlet ports, one attached to a bubbler and the other attached to a drierite column outside the chamber. Both the bubbler and drierite column were connected to solenoids that alternated the respective air flows into the chamber to vary the humidity that was controlled by a hygrometer located inside the environmental chamber. The DCB humidity was controlled in the relative humidity (RH) range of 3 to 98±0.3% at a temperature of 20°C.

Standard weights were added via a cage that was suspended below the environmental chamber to increase the stress intensity factor, K_I, as calculated from the strain energy release rate, $\mathcal{G}$ in equation 3. Approximately 600g was added to the sample cage with the notched sample held at 30% RH to form the initial crack at the center of the machined gap. Once the initial crack was formed, the RH of the chamber was adjusted to the desired level and more weights were added to increase K_I. Since the crack velocity is independent of crack length in the constant moment DCB setup, weight had to be added to

increase the crack velocity to characterize Region I and Region II v-K_I behavior. The environmental chamber, weights and DCB assembly are shown in Figure 2.1.

Figure 2.1: Environmental chamber and DCB assembly used to measure crack velocity at different stress intensities.

Crack velocity was measured using an optical system that included an objective lens (20X) on a Basler ACA150-UC camera (Exton, Pennsylvania) that collected images at up to 150 frames per second. ImageJ (version 1.41, U.S. National Institute of Health) was used to measure the crack length from videos recoded during testing.[44] Crack velocity was calculated from crack length and time between individual frames. Crack velocity was calculated from an average crack extension recorded over at least five different frame sets and used to produce velocity standard deviations for each of the K_I values.

Crack velocity in Region III was measured using a Phantom T4040 high speed camera (Wayne, New Jersey) that collected videos from 50,000 to 80,000 frames per

second which were also analyzed by ImageJ. Tapered samples (Figure 2.2) were used for the Region III testing. Because of the very high crack velocities encountered in Region III, the taper on the sample caused the moment of inertia to increase as the crack traveled down the sample, providing a range of K_I values over which crack velocity could be measured.

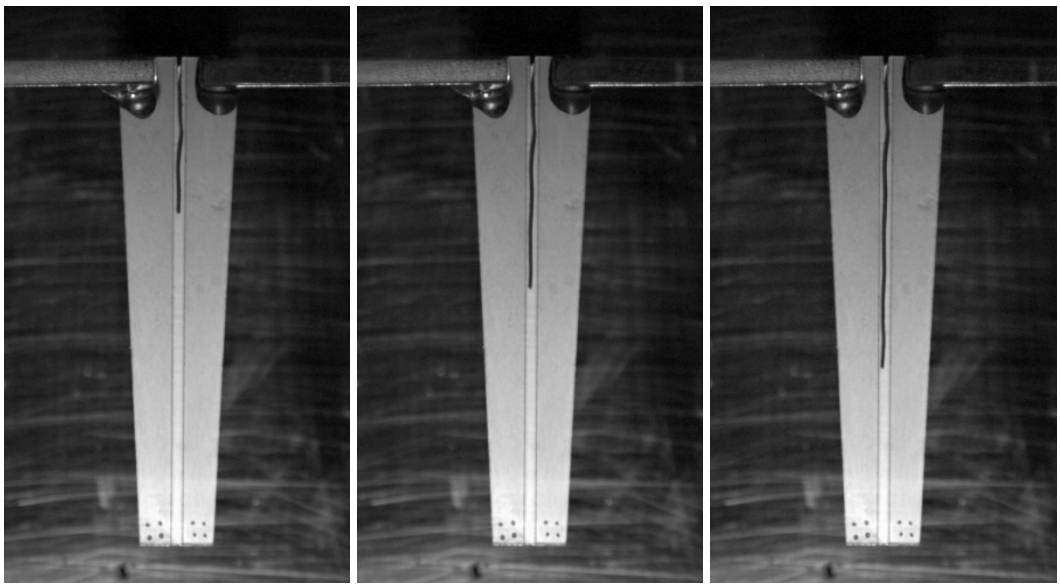

Figure 2.2: Tapered DCB samples used for measuring Region III crack growth velocities for the Schott-8061 glass samples.

2.3. TWO-POINT BEND TESTING

Fiber failure strains were measured using a two-point bending system (TNL Tool and Technology, LLC, Parnell IA), in deionized water at 20°C and in 20°C air at different values of RH. As was done for the DCB samples, an environmental glove box was built to fully encase the TPB setup to control RH. Gloves were added to the TPB environmental chamber (Figure 2.3, left) to ensure RH control during testing. The hygrometer for this

setup was located near the TPB fixture and on opposite sides of the chamber as the air inlets to ensure circulation of the humid air throughout the box, to again control the air humidity at 3 to 98±0.7% RH at 20°C.

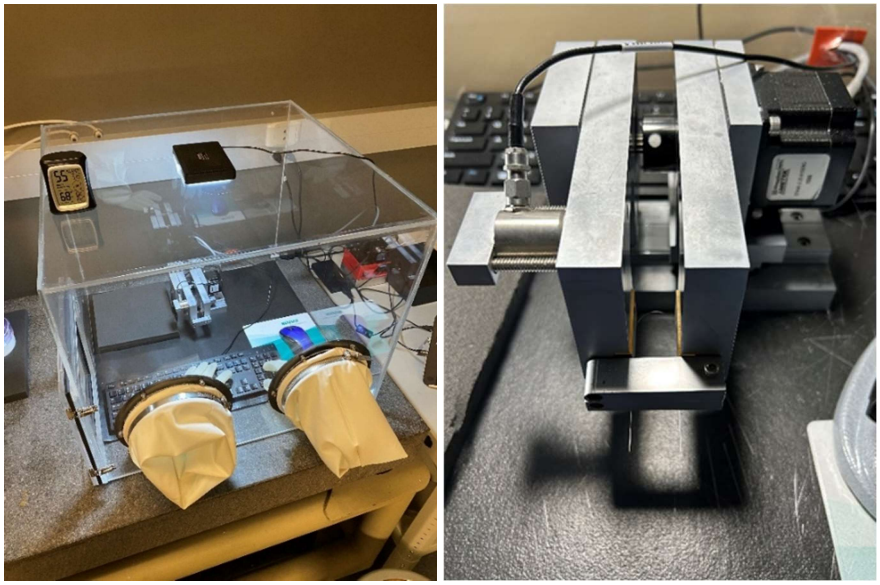

Figure 2.3: Environmental glove box used for the TPB tests on glass fibers in air with different values of RH.

Two-point bend (TPB) tests were done at constant faceplate velocities (v_{fp}), ranging from 5 to 4000µm/s. Failure strain (ε_f) was calculated from the faceplate gap at failure (D) and the fiber diameter (d) using Equation 10. A minimum of 20 fibers were tested for each set of experimental conditions and the two-point bending failure strain results are presented using the Weibull formalism:

$$\ln \ln \left(\frac{1}{(1-P)}\right) = m \ln \varepsilon_f \qquad [12]$$

where P is the probability of failure and m is the Weibull modulus, a dimensionless parameter related to the distribution of failure strains. The dynamic fatigue parameter

(n_{TPB}) was calculated from the faceplate velocity dependence of the failure strains measured in DI water and air using Equation 11.

2.4. GLASS PROPERTIES

Glass transition temperatures were determined by Differential Scanning Calorimetry (DSC), using a (Netzsch DSC 404). Glass powders (100-120 μm) were heated in air at a rate of 10°C/min, and the estimated uncertainty of the T_g values is ±2°C.

Thermal Mechanical Analyses (TMA) were done using a Netzsch TMA 402 F1 to characterize the coefficient of thermal expansion (CTE) and the glass transition temperature of each sample. Glass samples were cut into rectangular prisms (Table 2.2), with parallel top and bottom faces. The samples were then placed vertically between two alumina spacers and a load was applied by the TMA piston rod. The sodium silicate glasses were heated in air at a ramp rate of 3°C/min, and the Schott 8061 sample was heated in air at 5°C/min, each to their respective dilatometric softening points. CTE values were calculated between 100 and 400°C, with an uncertainty of 5.68×10^{-7}/°C; the uncertainty of the T_g values is ±2°C.

Resonant ultrasound spectroscopy (RUS) was done to measure the elastic modulus of the Schott-8061 and sodium silicate glasses. RUS measures the mechanical resonance of a freely vibrating body with a specified geometry. The rectangular sample was corner-mounted between two piezoelectric transducers and the samples were excited by a signal applied to one of the transducers. The applied signal has a range of frequencies all resonant responses were detected by the receiving transducer, then used to calculate the elastic

properties.[45] Measurements were made three separate times and average property values are reported.

2.5. FRACTURE TOUGHNESS

The fracture toughness was determined using the single-edged pre-crack beam (SEPB) method, described in ASTM C-1421.[46] The SEPB samples (Table 2.2) were cleaned with DI water, rinsed with ethanol, and then re-annealed to remove any residual stress resulting from machining. A Zwink test control II automated indenter was used to create nine Vickers indents laterally along the center of the bottom surface of each sample. Indents were produced with 9.81N load, held for 15s, and evenly spaced 0.3 mm apart from one another. Indented samples were then loaded in a bridge cracking assembly with 6 mm gap, shown in Figure 2.4. A load was applied to the assembly using an Instron 5565 5kN load cell at 0.05 mm/min. The load was removed when a crack popped in, as detected by an acoustic sensor. Samples were then removed from the bridge pre-crack assembly and gently placed into a common 4-point flexure loading fixture (Wyoming test fixture), shown in Figure 2.5. Here the load was applied until failure using an Instron 5565 1kN load cell at 0.05 mm/min. Both pre-crack and failure loading were conducted in dry N_2 atmosphere with relative humidity below 0.8% and a temperature of 25°C. Fractographic analyses were conducted on the fracture surfaces of each sample to measure the pre-crack length, which was used to calculate fracture toughness. Fractography was conducted on a Keyence VHX-7000, utilizing a VH-Z20R lens with x20-x200 magnification. Eight samples of each composition were tested and then averaged to determine the fracture toughness for the

composition, with an uncertainty of ±0.05 MPa*$m^{1/2}$. The K_{IC} values were used to with the K_I measurements from the DCB tests in the power law calculations described below.

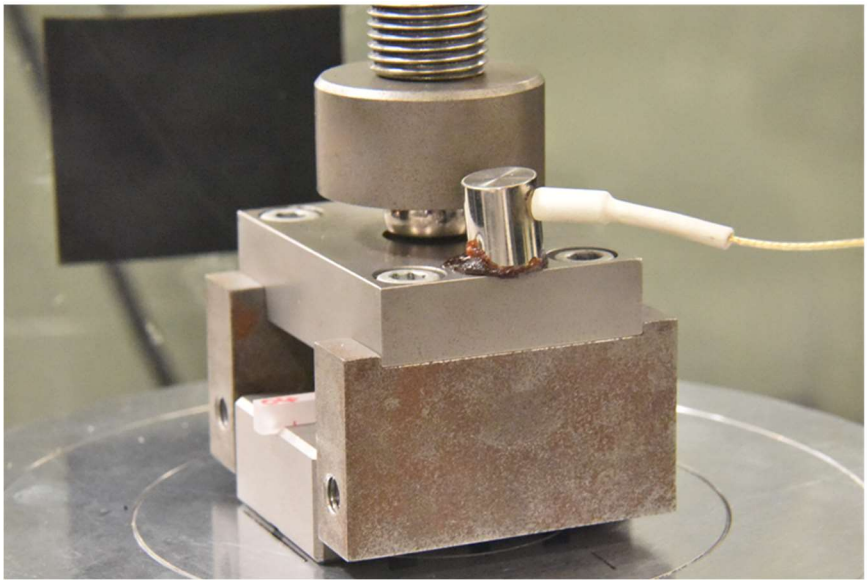

Figure 2.4: Bridge pre-crack assembly with 6 mm center gap.

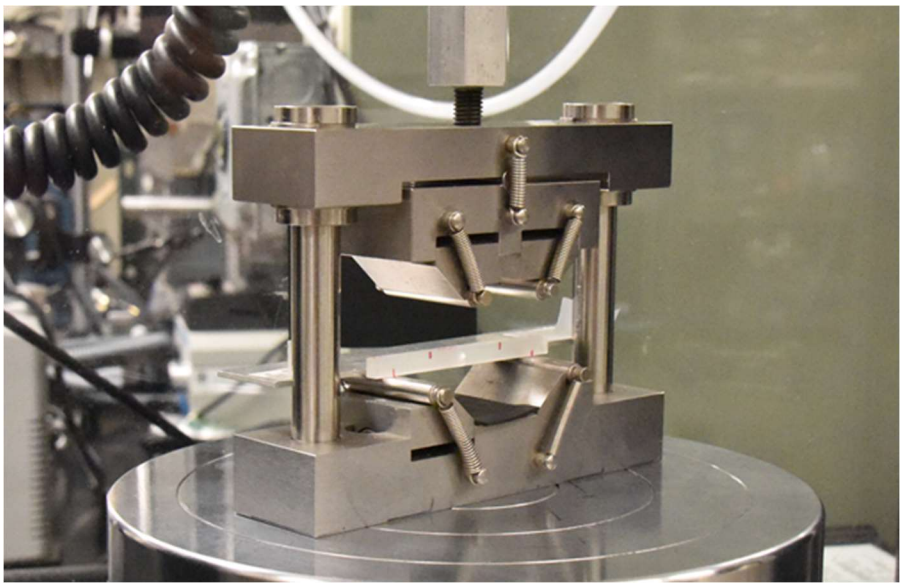

Figure 2.5: Common 4-point flexure loading assembly.

3. RESULTS AND DISCUSSION

3.1. GLASS PROPERTIES

Table 3.1 summarizes the thermal properties collected from the TMA and DSC analyses of the Schott-8061 and the sodium silicate glasses. With increasing soda contents, there is a decrease in T_g and an increase in coefficient of thermal expansion (CTE), consistent with trends reported in the literature.[47]

Table 3.1: CTE (100-400°C) and T_g values for the sodium silicate glasses and Schott-8061, measured by TMA and DSC.

Glass	TMA CTE (/°C)	TMA T_g (°C)	DSC T_g (°C)
$15Na_2O•85SiO_2$	$7.9x10^{-6}$	478	488
$25Na_2O•75SiO_2$	$12.4x10^{-6}$	470	473
$35Na_2O•65SiO_2$	$15.3x10^{-6}$	448	452
Schott-8061	$10.3x10^{-6}$	458	460

3.2. MECHANICAL PROPERTIES

Table 3.2 shows the elastic modulus and fracture toughness values for each of the glass compositions that were tested. There was a systematic increase in elastic modulus with increase in soda content as seen in the sodium silicate glass series. The increase in elastic modulus for Schott-8061 could be a result of the several other elements present in the glass. The fracture toughness value for Schott-8061 was similar to that reported Salem.[48] There is no statistical difference in the fracture toughness values of the three soda silicate glasses.

Table 3.2: Elastic modulus and fracture toughness values determined for the silicate glasses.

Glass	Elastic Modulus (GPa)	Density (g/cm^3)	Fracture Toughness ($MPa*m^{1/2}$)
$15Na_2O•85SiO_2$	62.5	2.34±0.02	0.72±0.06
$25Na_2O•75SiO_2$	62.9	2.42±0.02	0.69±0.05
$35Na_2O•65SiO_2$	63.0	2.34±0.01	0.71±0.05
Schott-8061	67.7	2.64±0.07	0.72±0.02[48]

3.3. SUBCRITICAL CRACK GROWTH

All three regions of SCCG were measured for Schott-8061 glass. For Regions I and II, the measurements were done using the Basler camera; however, because the crack velocities in Region III were much greater, the Basler camera frame rate was not able to record crack velocities that high. For that reason, the Phantom high-speed camera was used on tapered samples to measure Region III crack velocity. Figure 3.1 summarizes all three regions of Schott-8061 and the associated K_{IC} from literature.

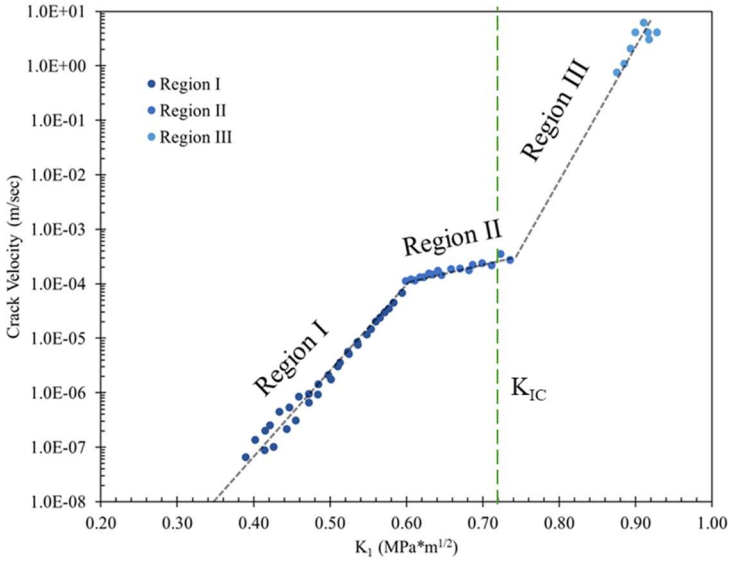

Figure 3.1: Regions I, II, and III of SCCG for Schott-8061, tested at 75% RH in 20°C air.

Figure 3.2 shows some of the detailed data for the Region II crack velocity for the Schott-8061 glasses. In general, Region II crack velocities were greater when tests were done at greater values of atmospheric RH. Wiederhorn reported similar RH dependences for Region II crack velocities in soda-lime silicate glasses; viz., Figure 1.4.[22]

A fatigue parameter was calculated from the Region II DCB data as the exponent of the logarithmic trendline. The data shown in Figure 3.2 indicates similar slopes, that are independent of RH, a finding that is consistent with those reported by Wiederhorn.[18] Wiederhorn reasoned that the corrosive attack that propagates a crack in Region I continues in Region II, but the plateau occurs because the crack speed controlled by the rate of water diffusion to the crack tip.[18] The increase in the magnitude of the Region II crack velocity with increasing RH at a constant value of K_I appears to be related to the increase in the K_I value where the transition for Region I to Region II occurs.

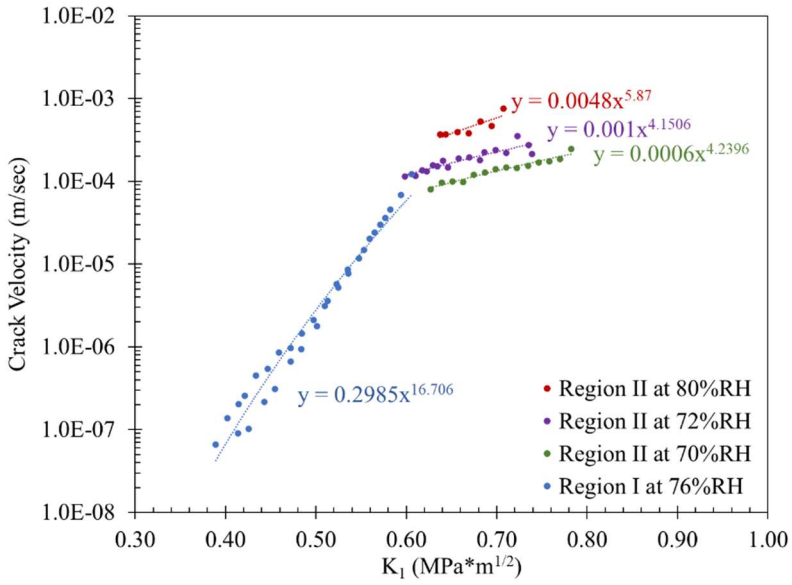

Figure 3.2: Regions I and II of SCCG for Schott-8061 glass tested in air with different relative humidity.

Figure 3.3 shows that the transition from Region II to Region III crack growth behavior for the Schott-8061glass occurs at a value of K_I greater than what was measured by the SEPB method. Results reported in the literature generally indicate a smaller range of Region III K_I values for than are shown in Figure 3.3. Uncertainties with the crack velocity and K_I measurements could be associated with the difficulty in analyzing the tapered sample and with the lower magnification of the phantom high-speed camera.

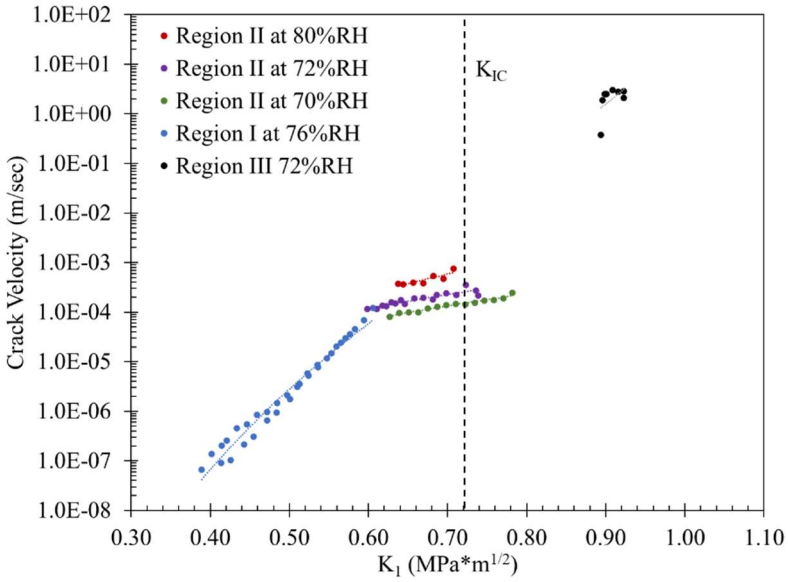

Figure 3.3: Regions I, II, and III crack velocity data for Schott-8061 tested in 20°C air at approximately 75% RH; the horizontal line is K_{IC} value measured by the SEPB method.

Only Region I crack velocities were measured for the binary sodium silicate glasses. The $35Na_2O$ composition was initially tested in 70±3% RH air but these conditions led to crack blunting and crack arrest because of rapid reactions between atmospheric water and the glass. When tested under 3±0.3% RH, stable crack growth behavior was noted for the $35Na_2O$ glass. When comparing the tests done in dry (3% RH) and wet (70% RH) air, there

was clear evidence for the presence of water, likely the result of capillary action, present at the crack tip in the latter samples. Figure 3.4a shows that water has filled the length of the crack driven into the $35Na_2O$ in a 70% RH air environment, whereas the tests done in dry air (3% RH) produced a sharper crack tip without noticeable pooling of water (Figure 3.4b). Condensation of water resulted in water inside the crack tip and throughout the crack body. This made it increasingly difficult to measure the crack front because the water distorted the crack tip, as seen in Figure 3.4c. In the 70% RH tests, the crack swayed from one side of the groove to the other repeatedly. By moving off centered the bending moment would change and as a result the K_I values measured would be different. When tested in dry environment the crack ran straight down the sample without swaying. Swaying of the crack tip in 70% RH for the $35Na_2O$ glass can be seen in Figure 3.4d.

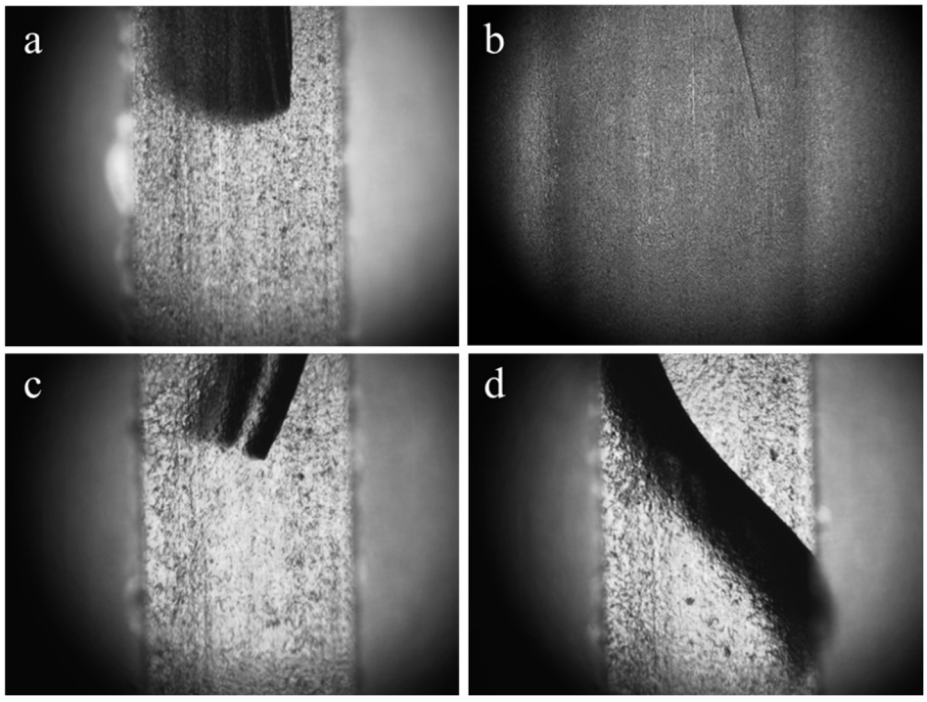

Figure 3.4: Crack tips in humid environment (a), crack tip in dry environments (b), water filling crack tip (c), and non-centralized swaying of crack tip (d) in $35Na_2O•65SiO_2$ glass.

The Region I DCB data are summarized in Figure 3.5 and include measurements from at least three different samples of each glass composition. The individual K_I values were calculated from the sample dimensions and the load applied during test. The v-K_I data in Figure 3.5 were used to calculate the SCCG parameters for each glass, based on the exponent of the logarithmic trendline.[42] The fatigue parameters are summarized in Table 3.3; here, a smaller value for n_{DCB} implies a greater sensitivity towards water for crack extension. The n_{DCB} value for Schott-8061 measured in this study (16.4 ± 1.2) is in good agreement with that reported from four-point bend test methods described by Salem and Tandon[48].

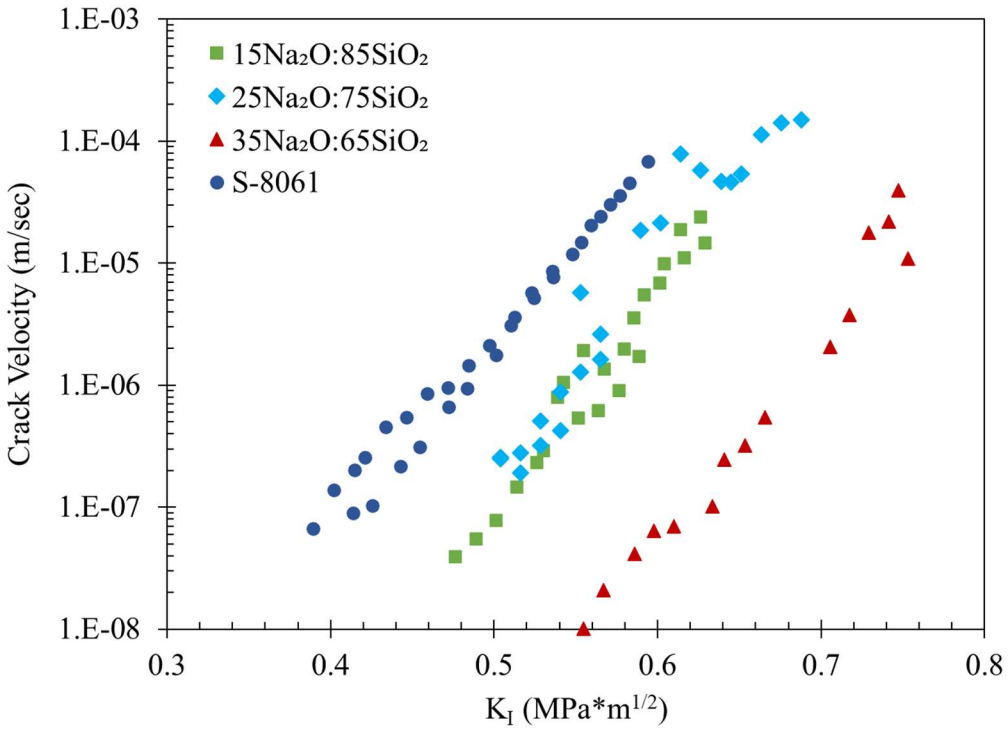

Figure 3.5: Crack velocity as a function of K_I for the various alkali silicate glasses, where Schott-8061, $15Na_2O$, and $25Na_2O$ were tested in ~70% RH air and $35Na_2O$ was tested in 3% RH air due to the blunting that occurred in high humidity.

Table 3.3: Fatigue parameters with 95% confidence intervals determined by DCB and TPB measurements for glasses in water or in humid air.

	n_{DCB} (70% RH air)	n_{TPB} (RT DI water)	n_{TPB} (70% RH air)
$15Na_2O•85SiO_2$	23.1 ± 1.3	10.5 ± 0.2	18.8 ± 0.3
$20Na_2O•80SiO_2$	--	--	12.2 ± 0.3
$25Na_2O•75SiO_2$	24.3 ± 1.7	7.4 ± 0.2	11.5 ± 0.3
$30Na_2O•70SiO_2$	--	--	11.2 ± 0.3
$35Na_2O•65SiO_2$	25.6 ± 1.0 (3% RH)	8.6 ± 0.2	10.4 ± 0.3
Schott-8061	16.4 ± 1.2	16.7 ± 0.3	18.6 ± 0.3

3.4. TWO-POINT BEND FAILURE STRAIN MEASUREMENTS AND DYNAMIC FATIGUE

Figure 3.6 shows the TPB failure strain distributions, plotted using the Weibull formalism, for $25Na_2O•75SiO_2$ glass fibers tested at increasing faceplate velocities (v_{fp}) in 20°C air at 70% RH. There is a systematic increase in failure strain with increasing v_{fp}, consistent with SCCG effects influencing the failure conditions.[40] Similar trends are apparent for the other glass compositions tested in both humid air at 70% RH and tested in 20°C DI water; viz., Figure A.3 and Tables A.2 and A.3 in the appendix. It can be seen that the failure strain for samples tested in water fell below the failure strain of samples tested in high humidity. This trend was observed with each of the glass compositions in each of the different testing setups.

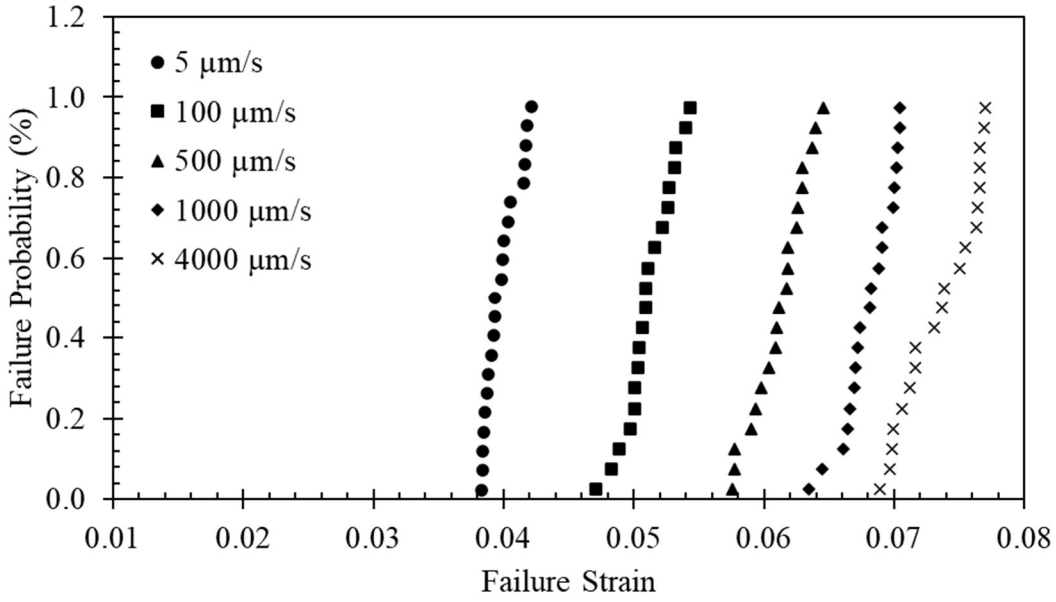

Figure 3.6 Two-point bend failure strain measurements made at various faceplate velocities in air (70% RH) for the $25Na_2O•75SiO_2$ glass fibers.

Figure 3.7 shows the average TPB failure strains as a function of soda concentration and faceplate velocity. There is a systematic increase in failure strain with increasing soda contents for tests done at 4000µm/s, a less systematic increase for the 500µm/s data, and almost no difference in failure strains of these glasses when measured at 5µm/s.

Celarie et al. studied ion diffusion in soda-lime silicates at the crack tip, in highly stressed regions. They claimed that there are two steps in slow crack growth: the first being fast migration of sodium ions to the fracture surface followed by a slower interdiffusion between the alkali ions and the hydronium ions enhanced by the network changing the bond angle and length under stress.[49] For the case of two-point bending, at the slower faceplate velocities which take much longer to test, a similar reaction may be taking place. Since the fibers have a pristine surface and no initial flaws, this stress-induced

reorganization of the silicate network could lead to the nucleation of a flaw, whereas DCB is the propagation of a macroscopic flaw initially present in the sample.

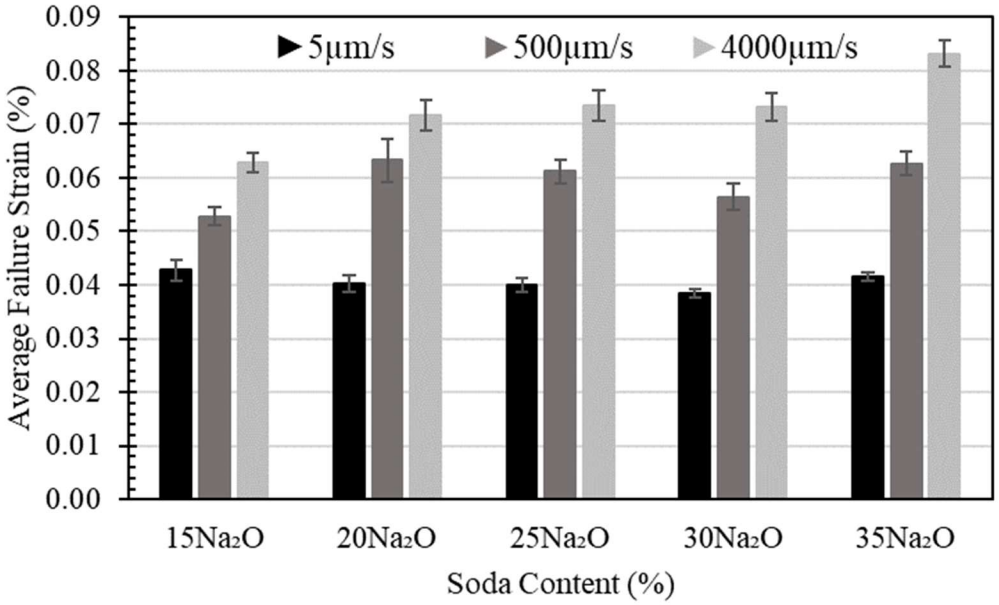

Figure 3.7: Average failure strains as a function of soda contents for binary soda silicate glass fibers tested in 20°C air at 70% RH.

The average failure strains for the sodium silicate fibers tested in 20°C DI water are shown in Figure 3.8. As was found for fibers tested in room temperature air at 70% RH (Figure 3.7), fibers tested in water at greater faceplate velocities had greater failure strains. There is little effect of glass composition on failure strains measured at different faceplate velocity. This is seen as the minimal change in failure strain with increase in soda content, which explain certain corrosion reactions that take place in highly reactive systems such as water, making the main mechanism of failure for the TPB samples tested in water different than those tested in high humidity.

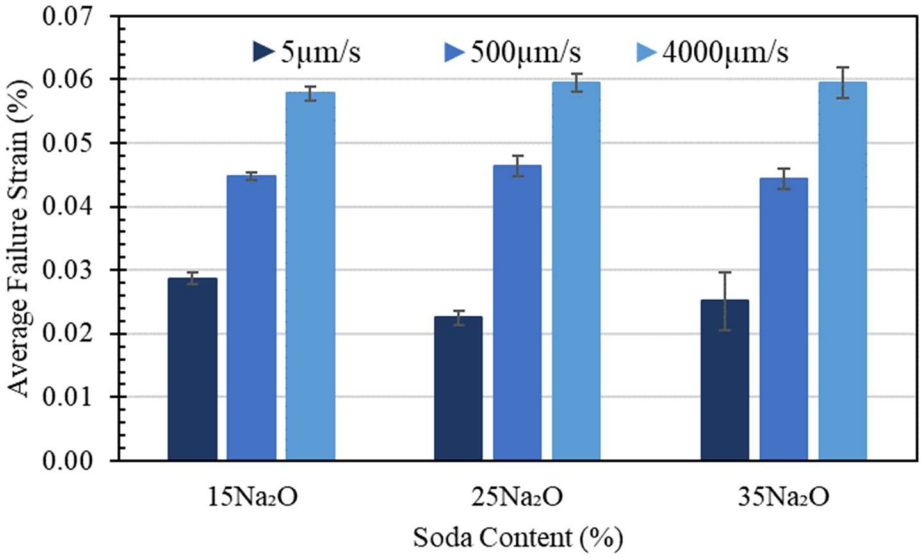

Figure 3.8: Average failure strains as a function of soda contents in the binary sodium silicate glasses for fibers tested in 20°C DI water.

Figure 3.9 shows the effects of faceplate velocity on the failure strains measured for $15Na_2O•85SiO_2$ glass fibers tested in both 20°C air at 70% RH and in 20°C DI water. Fibers failed at lower strains in water, although the differences between the failure strains for the two conditions were larger at slower faceplate velocities. Similar data sets were collected on the other glasses and are shown in Figure A.2 in the appendix.

The slope of the $\log(\varepsilon_f)$ vs. $\log(v_{fp})$ lines can be used to calculate the two-point bend fatigue parameter (n_{TPB}), from Eq.[11], and these values are equal to 18.8±0.3 for samples tested in 20°C air (70% RH) and 10.5±0.2 for samples tested in 20°C DI water. A lower value of the fatigue parameter indicates a greater sensitivity to the effects of water. Figure 3.10 summarizes the $\log(\varepsilon_f)$ vs. $\log(v_{fp})$ data for each glass tested in 20°C air (70% RH), and the resulting fatigue parameters are given in Table 3.3, along with those obtained from fibers tested in water. It is worth noting that the n_{TPB} measured here for the $25Na_2O•75SiO_2$

glass in water (7.4 ± 0.2) is in good agreement with the value reported by Tang (6.9 ± 0.2) for similar experimental conditions.[40]

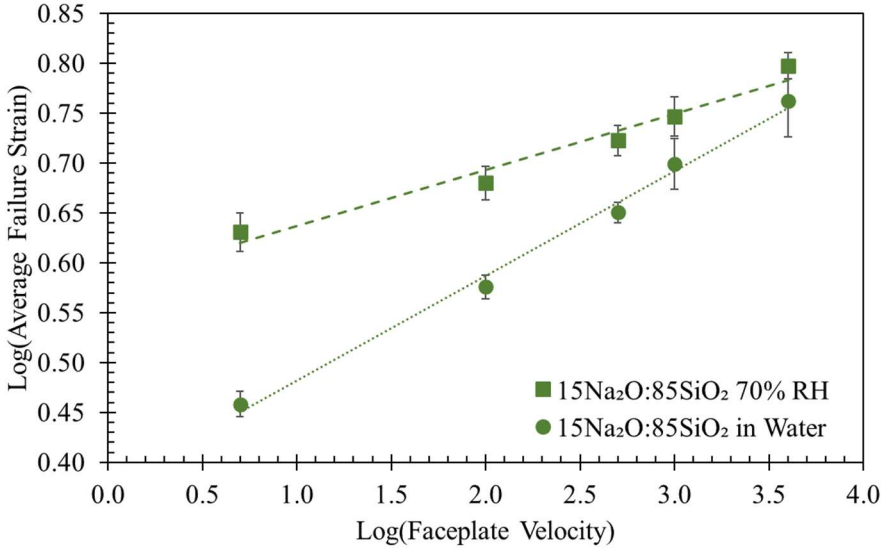

Figure 3.9: Log ε_f vs. log v_{fp} for $15Na_2O{\bullet}85SiO_2$ glasses tested in both 20℃ air at 70% RH and in 20℃ DI water.

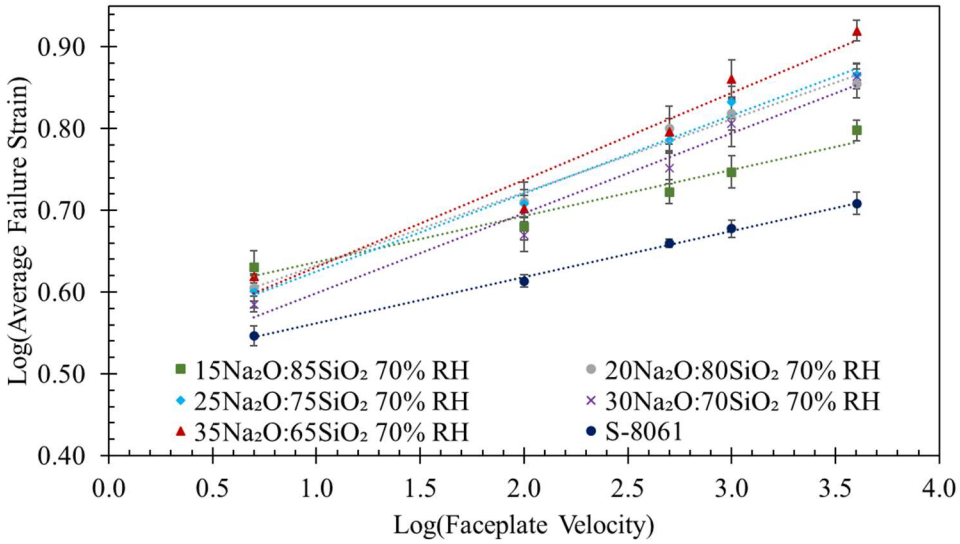

Figure 3.10: Average failure strain as a function of faceplate velocity for each glass measured in 20℃ air at 70% RH.

The stress intensity dependence of Region I crack velocity measured by TPB can be modeled with a power law, as described by ASTM C1368:[50]

$$v = \frac{da}{dt} = AK_I^{n_{TPB}} = A^* \left(\frac{K_I}{K_{IC}}\right)^{n_{TPB}} \quad [13]$$

where A* is the slow crack growth parameter and is calculated from:

$$A^* = \frac{2K_{IC}^2 \sigma_i^{\left(\frac{1}{\alpha}-3\right)}}{10^{\beta/\alpha}(1-3\alpha)Y^2} = \frac{2K_{IC}^2}{B(n_{TPB}-2)Y^2} \quad [14]$$

where Y is geometry factor related to the flaw shape (equal to 1.122 for semicircular flaws in bending)[51], B is the material/environmental parameter, n_{TPB} is the fatigue parameter discussed above, and α and β are the slope and y-intercept of the log(flexure strength) vs. log(stress rate). Rondinella and Mattewson[42] used this power law model to analyze TPB data. From log(ε_f) vs log(v_{fp}) data, like those shown in Figure 3.10. The slope was used to calculate a fatigue parameter (n_{TPB}, Equation 11) and the intercept (β) was used to calculate the B-term in Equation 14 from:

$$B = \frac{Er(n_{TPB}+1)10^{\beta(n_{TPB}-1)}}{0.417(n_{TPB}-1)} \quad [15]$$

where E is the elastic modulus and r is the radius of the glass fiber. Table 3.4 shows the values for β and n_{TPB} from the linear regression analysis of the $\varepsilon_f(v_{fp})$ data shown in Figure 3.10. These values were then used to calculate the crack velocity-stress intensity relationships for different glasses tested under the TPB conditions, using equation 13, but with n_{TPB}. Figure 3.11 shows the results of those calculations for each glass composition that has pairing DCB data.

Table 3.4: Power law parameters calculated from TPB failure strain measurements in 70% RH air.

	β	n_{TPB} (70% RH air)
$15Na_2O•85SiO_2$	0.58 ± 0.02	18.8 ± 0.3
$20Na_2O•80SiO_2$	0.54 ± 0.02	12.2 ± 0.3
$25Na_2O•75SiO_2$	0.53 ± 0.02	11.5 ± 0.3
$30Na_2O•70SiO_2$	0.50 ± 0.02	11.2 ± 0.3
$35Na_2O•65SiO_2$	0.52 ± 0.02	10.4 ± 0.3
Schott-8061	0.51 ± 0.01	18.6 ± 0.3

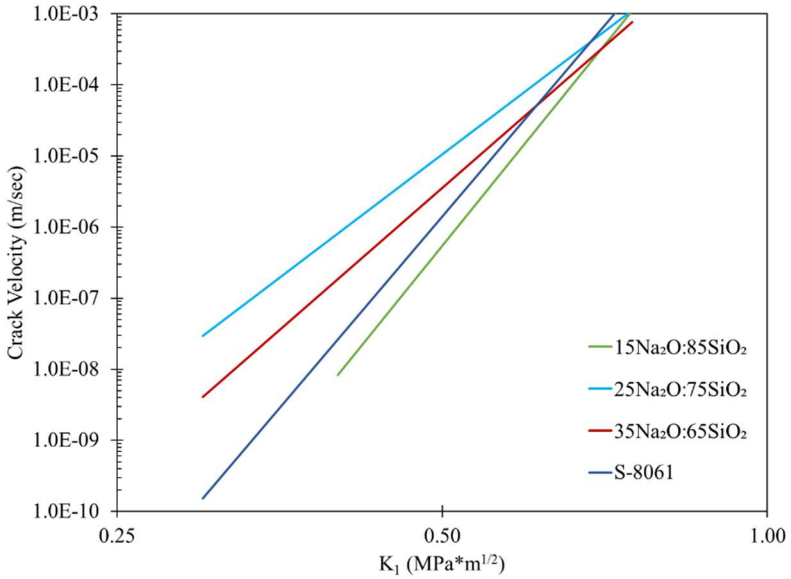

Figure 3.11: Region I crack velocities for alkali silicate glasses in room temperature air at 70% RH, calculated from the TPB parameters in Table 3.1 and Eq. 13.

Figure 3.12 compares the Region I crack velocities calculated from the TPB parameters (lines) to the respective crack velocities measured by DCB (symbols) for the $15Na_2O•85SiO_2$ glass (left) and for Schott-8061 (right). The power law model (Equations 13-15) does a good job of reproducing the relative magnitudes of the DCB V-K data from

the TPB parameters, but the differences in slopes of the two data sets reflect the differences in n_{DCB} and n_{TPB}, particularly for the $15Na_2O•85SiO_2$ glass (Table 3.3).

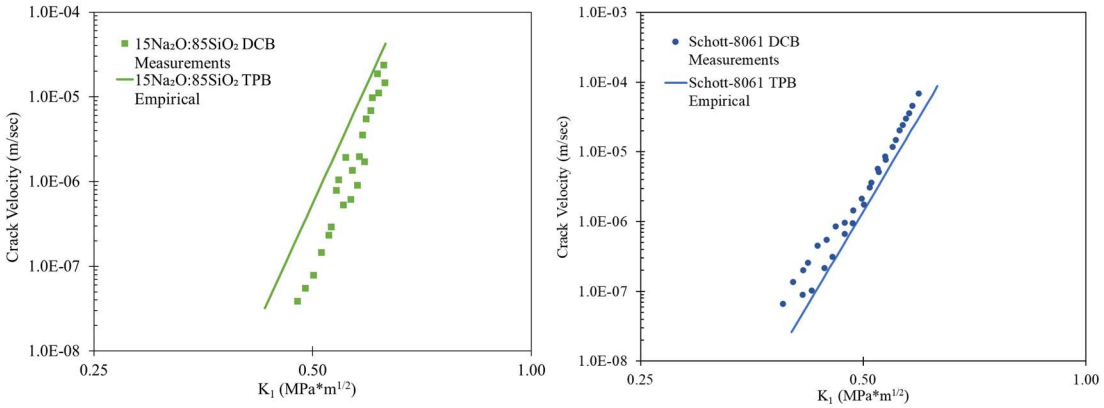

Figure 3.12: Region I V-K data in 70% RH air for (left) $15Na_2O•85SiO_2$ glass, and (right) Schott-8061 glass. Symbols are measured by DCB and lines are predicted by TPB.

In comparison to the fatigue parameters from the DCB measurements in Table 3.3, those obtained by TPB are all lower, indicating a greater sensitivity towards water for TPB failure than for crack extension in the DCB tests. In addition, the more chemically durable glasses (Schott-8061 and $15Na_2O•85SiO_2$) have greater values of n_{TPB}, measured in water and in 70% RH air, than what was measured for the less durable glasses ($25Na_2O•75SiO_2$ and $35Na_2O•65SiO_2$), whereas those less durable glasses have greater values of n_{DCB}. This suggests that the effects of water on crack extension, as measured by DCB, are different from the effects of water on inducing failure in a TPB experiment.

When sodium silicate glasses are exposed to water or water vapor, an ion exchange reaction can occur at the surface to release sodium ions to the solution and to create a silica gel surface layer;[52] viz., reactions [8] and [9]. Charles and Hillig[16] found that under subcritical K_I conditions, reactions between the glass and atmospheric water caused the

crack tip radius to broaden and thus blunt crack growth, a phenomenon also noted by Ito and Tomozawa.[53] Gehrke et al. found that the formation of a leached layer on corroded alkali silicate glasses arrested Vickers indentation cracks.[54] Similar effects could explain the high values of n_{DCB} found in this study for the soda-rich silicate glasses and why stable crack growth was not found for the $35Na_2O$ glass at 70% RH. In the 70% RH sample, condensation was observed to well up in the crack tip (Figure 3.4a) and this could lead to crack blunting, whereas in the 3% RH test there was a sharp crack tip throughout the entirety of the tests.

The fatigue parameters for TPB were collected under dynamic testing conditions where the specimens are loaded to failure (i.e., increasing stress intensity), whereas the Region I DCB conditions do not reach the critical stress intensity for failure. As a consequence, the longer times associated with the DCB measurements allow for greater interactions between water and the crack tip, altering the conditions for crack extension.

A second difference between the DCB and TPB experiments is the nature of the flaw that leads to sample failure. In the DCB tests, the critical flaw is machined into the sample and then extended by increasing the applied load. Water accelerates the flaw extension for a given applied load. In the TPB experiments, the surfaces of fibers drawn from the melt are much more pristine, and the fibers must withstand significantly greater loads before they fail than those that are applied in a DCB experiment. The role of water under the TPB conditions may be to first nucleate a flaw and then propagate it to failure.[55] The lower values of n_{TPB} for the soda-silicate glasses, in both water and in 70% RH conditions, may indicate the greater sensitivity of these glass surfaces for the water-induced nucleation of the initial flaw.

Lower et al. reported that the failure strains from binary soda-silicate glasses tested in liquid nitrogen increased systematically with increasing soda contents and glasses with more than 10 mole% Na_2O had greater failure strains at lower faceplate velocities.[56] Fatigue effects are removed for tests under liquid nitrogen and so the failure strain trends noted by Lower, et al. were associated with a greater reorganization of the modified silicate network for glasses with greater soda contents. In a recent molecular dynamics study, Kob et al.[57] noted similar compositional dependences on failure strain behavior of binary soda silicate glasses under tension and related that to strain-induced deformations of the silicate network and distortions of the bonding environments around the sodium ions. Similar structural reorganization effects may contribute to the overall greater failure strains of the alkali-rich binary glasses, compared to glasses with more cross-linked silicate networks, i.e., Figure 3.9. It is conceivable that the reorganization of the network structure under the much greater loads applied in a TPB experiment may determine the conditions under which an ultimately fatal flaw is nucleated on the pristine glass surface.

4. CONCLUSIONS

The DCB method was found to be useful for measuring stable crack growth velocities in all three regions of subcritical crack growth, although the $35Na_2O•65SiO_2$ samples tested in 70% RH air exhibited crack arrest due to water penetrating and blunting the crack tip. When tested in 3% RH air, stable crack growth was observed. Two-point bend studies performed in DI water and in air were able to produce consistent strain measurements and high Weibull moduli. Failure strain measurements were used to calculate dynamic fatigue parameters for each of the glass compositions in 70% RH air and it was determined glasses with greater soda-contents were more sensitive to the effects of water (lower values of n_{TPB}). In contrast, to the DCB measurements which revealed less sensitivity to water (greater values of n_{DCB}) for the alkali rich glasses. An empirical power law model was used to predict Region I crack velocities from the TPB data and these reflected the differences in n_{DCB} and n_{TPB}. The DCB experiments measure the extension of pre-existing flaws and are sensitive to changes in the local environment of the crack tip which can alter flaw geometry and thus change the V-K characteristics. The TPB measurements, on the other hand, are made on pristine glass fibers and the effects of water on the nucleation of the critical flaw may control the fatigue behavior.

5. FUTURE WORK

This research has demonstrated the feasibility of measuring subcritical crack growth of the Schott-8061 glass in 70% RH air for all three regions. However, for less chemically stable glasses like the binary sodium silicate glasses, only Region I data could be obtained at 70% RH. To further improve the understanding of fatigue susceptibility and subcritical crack growth, DCB and TPB should be tested under lower humidity conditions.

The procedures for DCB testing followed in the present work could be improved. Initial DCB tests of the $15Na_2O•85SiO_2$ glass at 3% RH produced hairline cracks that could not be analyzed using current procedures. It was found that polishing the back of the DCB sample and the DCB sample groove, both to a 1μm finish, then imaging the resulting cracks at a greater magnification than used before, allowed quantitative crack velocity measurements to be made. Figure 5.1. shows an example of the improved resolution for characterizing DCB cracks.

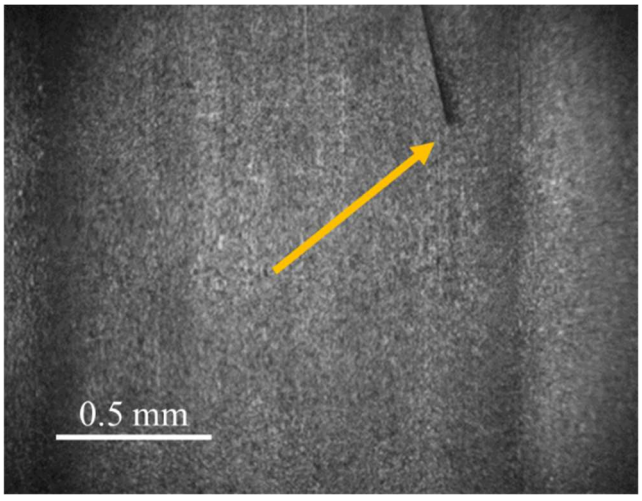

Figure 5.1: Sharp crack tip of $25Na_2O•75SiO_2$ composition tested in 20°C air at 3% RH after the surface had been polished.

To better understand the humidity dependence of the TPB failure strains, TPB testing should be done in air under a wider range of relative humidity values. Figure 5.2 shows the humidity dependence of failure strain for silica, soda-lime silicate, and E-glass, reported by Tang et al.[40]. Similar data collected on the binary soda silicate glasses might separate contributions to failure strain from structural reorganization effects from those associated with fatigue reactions with strained bonds in pristine glasses.

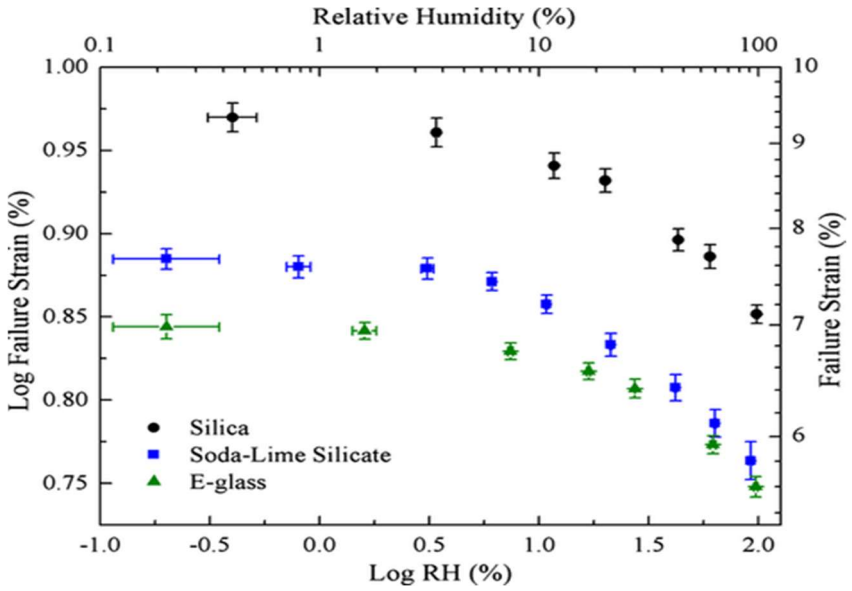

Figure 5.2: Failure strain in air as a function of relative humidity for commercial silicate glasses; from Tang et al.[40]

By further investigating strain and subcritical crack growth, a better understanding of fatigue in both short-term and long-term testing can be obtained, and this understanding could be useful for those who need to predict the lifetimes of glass components.

APPENDIX

Table A.1: Temperatures used for pulling fibers from glass composition.

Glass composition	Fiber puling temperature (°C)
$15Na_2O•85SiO_2$	1150
$20Na_2O•80SiO_2$	1075
$25Na_2O•75SiO_2$	1020
$30Na_2O•70SiO_2$	900
$35Na_2O•65SiO_2$	850
Schott-8061	1170

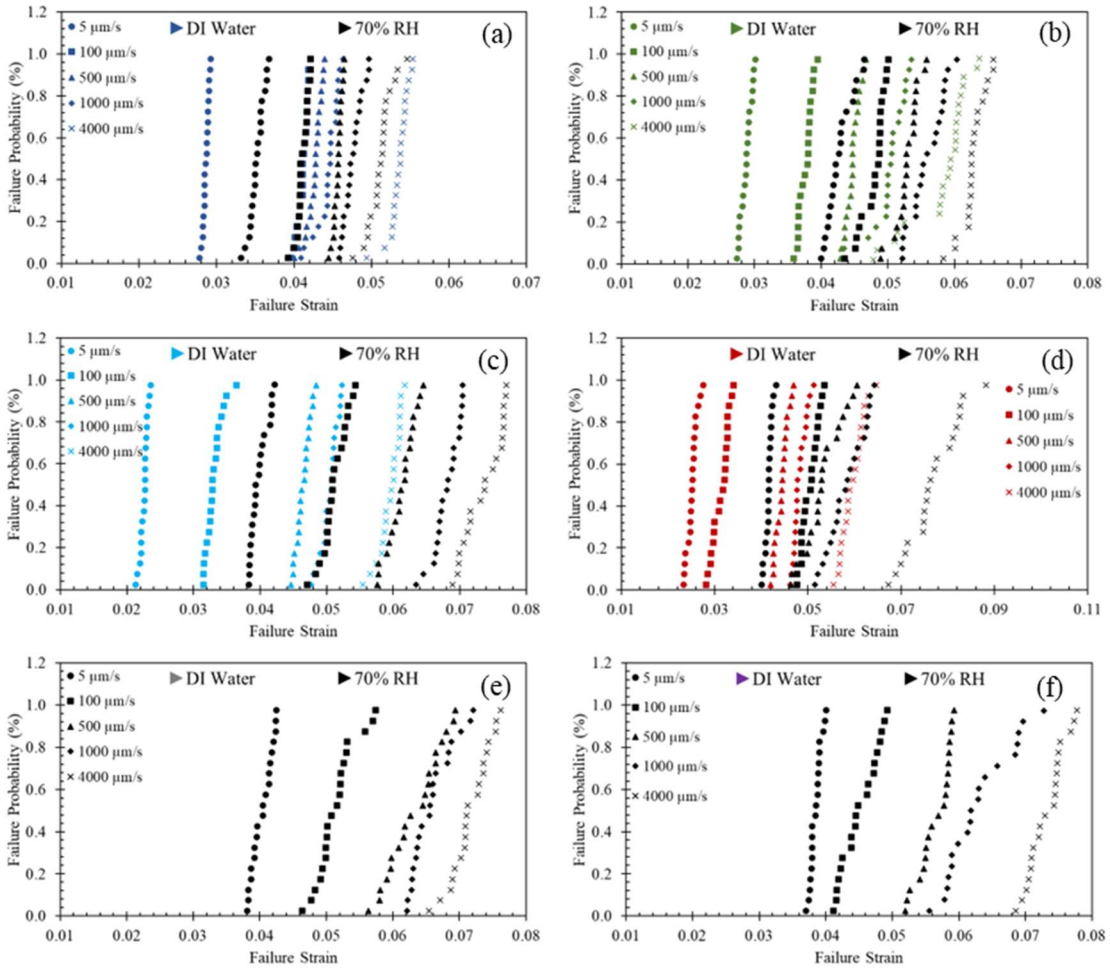

Figure A.1: Two-point bend failure strain measurements made at various faceplate velocities in air (70% RH) and DI water at 20°C for (a) Schott-8061, (b) $15Na_2O•85SiO_2$, (c) $25Na_2O•75SiO_2$, and (d) $35Na_2O•65SiO_2$ (e) $20Na_2O•80SiO_2$, (f) $30Na_2O•70SiO_2$ glass compositions.

Table A.2: Average two-point bend failure strain measurements made at various faceplate velocities in 20°C air (70% RH) for all glasses tested.

	Failure Strain at 5μm/s	Failure Strain at 100μm/s	Failure Strain at 500μm/s	Failure Strain at 1000μm/s	Failure Strain at 4000μm/s
$15Na_2O•85SiO_2$	4.27±0.19	4.79±0.18	5.28±0.18	5.59±0.25	6.28±0.19
$20Na_2O•80SiO_2$	4.04±0.15	5.14±0.29	6.32±0.40	6.59±0.31	7.16±0.29
$25Na_2O•75SiO_2$	3.99±0.13	5.11±0.19	6.12±0.21	6.80±0.20	7.35±0.29
$30Na_2O•70SiO_2$	3.84±0.08	4.68±0.23	5.64±0.24	6.41±0.42	7.32±0.27
$35Na_2O•65SiO_2$	4.16±0.08	5.04±0.18	6.26±0.22	7.26±0.40	8.31±0.24
Schott-8061	3.52±0.10	4.11±0.07	4.57±0.05	4.76±0.12	5.11±0.16

Table A.3: Average two-point bend failure strain measurements made at various faceplate velocities in 20°C DI water for all glasses tested.

	Failure Strain at 5μm/s	Failure Strain at 100μm/s	Failure Strain at 500μm/s	Failure Strain at 1000μm/s	Failure Strain at 4000μm/s
$15Na_2O•85SiO_2$	2.87±0.09	3.77±0.10	4.47±0.11	5.01±0.28	5.80±0.45
$25Na_2O•75SiO_2$	2.26±0.06	3.31±0.13	4.45±0.16	5.04±0.13	5.95±0.17
$35Na_2O•65SiO_2$	2.52±0.11	3.14±0.18	4.44±0.14	4.83±0.14	5.95±0.24
Schott-8061	2.87±0.06	--	3.63±0.15	3.73±0.17	4.44±0.33

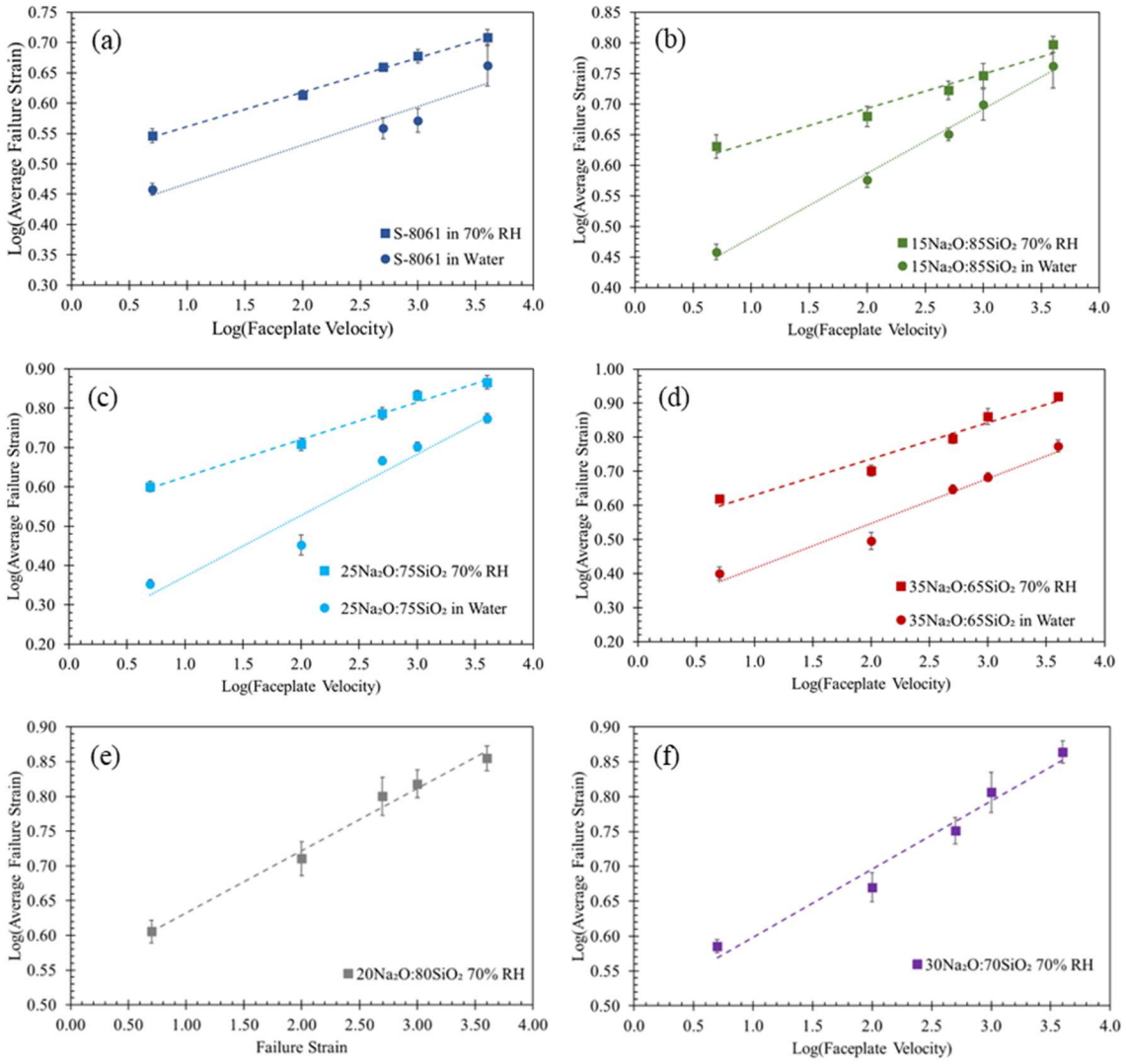

Figure A.2: Log ε_f vs. log v_{fp} for glasses tested in both 20°C air at 70% RH and in 20°C DI water, for (a) Schott-8061, (b) $15Na_2O•85SiO_2$, (c) $25Na_2O•75SiO_2$, and (d) $35Na_2O•65SiO_2$, (e) $20Na_2O•80SiO_2$, (f) $30Na_2O•70SiO_2$ glass compositions.

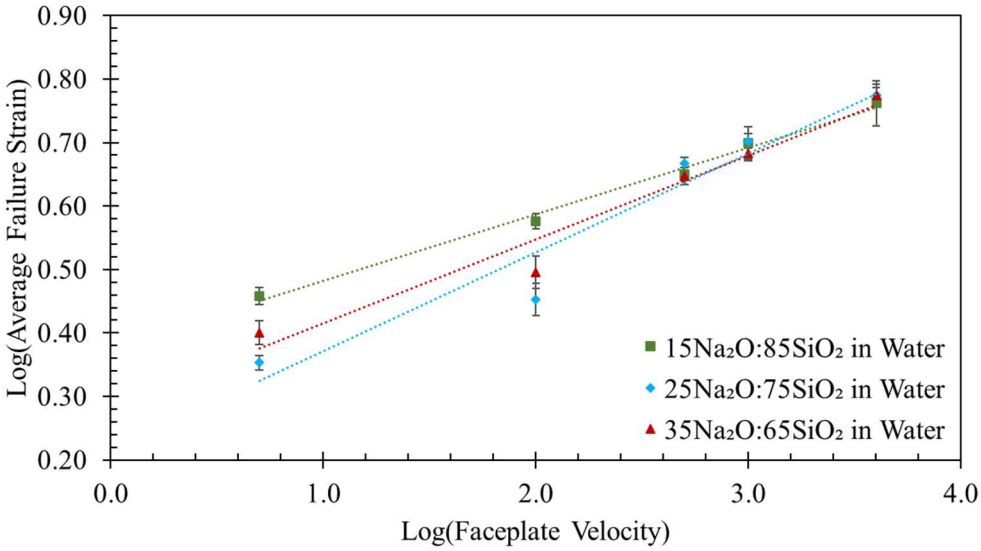

Figure A.3: Average TPB failure strains as a function of faceplate velocity for glasses measured in 20°C DI water.

REFERENCES

1. J. Rimsza, K. Strong , M. Buche, et al., *Sandia National Lab. (SNL-NM)*, SAND2022-12758710024, (2022).

2. R. C. Bradt, A. G. Evans, D. P. H. Hasselman, F. F. Lange, *Fracture mechanics of ceramics*, Volume 8, Microstructure, methods, design, and fatigue (1986).

3. C. R. Kurkjian, P. K. Gupta, R. K. Brow., *Int. J. Appl. Glass Sci*., 1(1):27 (2010).

4. W. L. Smith, T. A. Michalske. *Sandia National Lab*, (1993).

5. S. W. Freiman, D. R. Mulville, P. W. Mast., *J. Mater. Sci*., 8(11):1527 (1973).

6. A. K. Varshneya, *Fundamentals of Inorganic Glass*, Academic Press (1994).

7. J. B. Wachtman, W. R. Cannon, M. J. Matthewson., *Mechanical properties of ceramics*, 2nd ed., Wiley (2009).

8. E. J. Ripling, S. Mostovoy, R. L. Patrick, *Mat. Res. Stand.*, 4:129 (1964).

9. P. P. Gillis, S. A. Gilman, *J. Appl. Phys.* 35:647 (1961).

10. S. M. Wiederhorn, A. M. Shorb, R. L. Moses., *ibm*, 39:1569 (1968).

11. J. O. Outwater, M. C. Murphy, *Final Report Contract No. DAAA 21-67-C-0041* (1970).

12. J. A. Kies and A. B. J. Clark, *Proceedings of the Second International Conference on Fracture*, Paper 41 (1969).

13. C. H. Hsueh, E. Y. Sun, P. F. Becher, K. P. Plucknett, *J. Mater. Res.*, 13(9):2539 (1998)

14. S. M. Wiederhorn, *Subcritical Crack Growth in Brittle Materials: Mechanics, Encyclopedia of Materials* (2008).

15. C. Kocer, R. E. Collins, *J. Am. Ceram. Soc*., 84(11):2585 (2001).

16. R. J. Charles, W. B. Hillig, pp. 511-527 in "Symposium on Mechanical Strength of Glass and Ways of Improvising It," Florence, Italy, September 25-29 (1961).

17. W. B. Hillig, R. J. Charles, *High Strength Materials*, (Ed. V. F. Zackey), John Wiley and Sons, 682 (1965).

18. S. M. Wiederhorn, S. W. Freiman, E. R. Fuller, C. J. Simmons. *J. Mater. Sci*., 17(12):3460 (1982).

19. A. G. Evans, S. M. Wiederhorn, *Int. J. Fract.* 10:379 (1974).

20. S. M. Wiederhorn, H. Johnson, *J. Am. Ceram. Soc.,* 56:192 (1973).

21. M. Ciccotti, *J. Phys. D: Appl. Phys*., 42(21):214006 (2009).

22. S. M. Wiederhorn, *J. Am. Ceram. Soc*. 50, 407 (1967).

23. S. M. Wiederhorn, *J. Am. Ceram. Soc.*, 19:169 (1975).

24. D. R. Lide, *A Century of Excellence in Measurements, Standards, and Technology (1st ed.)*, CRC Press, (2002).

25. T. C. Baker, F. W. Preston, *J. Appl. Phys.*, 17(3):162 (1946).

26. T. C. Baker, F. W. Preston, *J. Appl. Phys.*, 17(3):170 (1946).

27. T. C. Baker, F. W. Preston, *J. Appl. Phys.*, 17(3):179 (1946).

28. B. R. Lawn, *J. Am. Ceram. Soc.*, 66(2):83 (1983).

29. T. A. Michalske, S. W. Freiman, *J. Am. Ceram. Soc*., 66(4):284 (1983).

30. A. T. Taylor, M. J. Matthewson, *Proc. Int. Wire & Cable Symp*., 47:874 (1998).

31. S. M. Wiederhorn, L. H. Bolz, *J. Am. Ceram. Soc.*, 53(10):543 (1970).

32. R. J. Charles, *J. Appl. Phys*., 29(11):1554 (1958).

33. R. H. Doremus, *J. Non-Cryst. Solids*, 19:137 (1975).

34. R. J. Charles, *J. Appl. Phys*., 29(11):1549 (1958).

35. R. J. Charles, *J. Appl. Phys*., 29(11):1554 (1958).

36. R. J. Charles, *J. Appl. Phys.,* 29(12):1657 (1958).

37. P. W. France, W. J. Duncan, D. J. Smith, K.J. Beales, *J. Mat. Sci*., 18:785 (1983).

38. C. R. Kurkjian, P. K. Gupta, *Phys. Chem. Glasses-B*., 61(6):239 (2020).

39. M. J. Matthewson, C. R. Kurkjian, S. T. Gulati, *J. Am. Ceram. Soc*., 69(11):815 (1986).

40. Z. Tang, R. K. Brow, *Int. J. Appl. Glass Sci*., 5(3):287 (2014).

41. R. J. Charles, *J. Appl. Phys*., 29(12):1657 (1958).

42. V. V. Rondinella, M. J. Matthewson., *J Am. Ceram. Soc*., 76(1):139 (1993).

43. E. A. Ronchetto, Doctoral Dissertations. 2845, *Missouri University of Science and Technology*, (2019).

44. W. S. Rasband, ImageJ, U. S. National Institutes of Health, Bethesda, Maryland, USA.

45. Z. Zhang, V. Keppens, P. K. Liaw, et al., *J. Mat. Res*., 22:364 (2007).

46. ASTM C1421-18, *Standard Test Method for Determination of Fracture Toughness of Advanced Ceramic at Ambient Temperature.*

47. M. Tomozawa, et al., *J. Non. Cryst. Solids*, 56(1-3):343 (1983).

48. J. Salem, R. Tandon, *Int. J. Fatigue*., 32(3):557 (2010).

49. F. Celarie, M. Ciccotti, C. Marliere, *J. Non-Cryst. Solids*, 353:51 (2007).

50. ASTM C1368-18, *Standard Test Method for Determination of Slow Crack Growth Parameters of Advanced Ceramics by Constant Stress Rate Strength Testing at Ambient Temperature.*

51. H. Tada, P. C. Paris, G. R. Irwin., *The stress analysis of cracks handbook. Third edition*. (2000).

52. T. A. Michalske, B. C. Bunker, *Sci Am*., 257(6):122 (1987).

53. S. Ito, M. Tomozawa, *J. Am. Ceram. Soc.,* 65(8):368 (1982).

54. E. Gehrke, C. Ullner, M. Mahnert, *J. Mater. Sci.,* 26:5445 (1991).

55. N. P. Lower, R. K. Brow, C. R. Kurkjian., *J. Non. Cryst. Solids*., 344(1–2):17 (2004).

56. N. P. Lower, R. K. Brow, C. R. Kurkjian., *J. Non. Cryst. Solids*., 349:168 (2004).

57. Z. Zhang, S. Ispas, W. Kob, *Phys. Rev. Materials.*, 6(8):085601 (2022).

VITA

Noah Weyrauch was born on December 9th, 1997, in Blue Springs, MO. He moved around Missouri before landing in Warrensburg, MO in 2010 where he attended Warrensburg High School. Noah graduated from Warrensburg in the spring of 2016 and began his college education at the University of Central Missouri (UCM) later that fall. He studied Biomedical Sciences for two years before transferring to the Missouri University of Science and Technology with a declared major in Ceramic Engineering. At Missouri S&T, Noah was a member of the Concrete Canoe Design Team where he held the position of chief engineer. In the spring of 2019, he joined the KERAMOS chapter of Missouri S&T. During his undergraduate career, Noah worked with Sandia National Laboratories as a year-round intern, virtually in Rolla and in Albuquerque, NM for two summers (2020 and 2021) to do research, some of which is described in this thesis. Noah received his B.S. degree in Ceramic Engineering from Missouri S&T in May of 2020.

Noah began his Masters graduate work in June 2020, under the supervision of Dr. Richard K. Brow at Missouri University of Science and Technology. During his graduate career, Noah focused his research on the understanding the subcritical crack growth behavior and the dynamic fatigue parameters in alkali silicate glasses. He was also a teaching assistant for the undergraduate ceramic processing lab, gave presentations at ICACC 2021, GOMD 2022, GOMD 2023, was a co-author on two Sandia National Laboratories internal reports, and published one paper, so far, on his research. Noah received his M.S. degree in Material Science and Engineering from Missouri University of Science and Technology in May 2023.